Understanding the role of anharmonic phonons in diffusion of bcc metals

Seyyedfaridoddin Fattahpour, Ali Davariashtiyani, and Sara Kadkhodaei*
Civil, Materials, and Environmental Engineering, University of Illinois Chicago, 2095 Engineering Research Facility, 842 W. Taylor St., Chicago, Illinois 60607, USA

(Received 20 December 2021; accepted 9 February 2022; published 28 February 2022)

Diffusion in the high-temperature bcc phase of IIIB-IVB metals such as Zr, Ti, and their alloys is observed to be orders of magnitude higher than bcc metals of group VB-VIB, including Cr, Mo, and W. The underlying reason for this higher diffusion is still poorly understood. To explain this observation, we compare the first-principles-calculated parameters of monovacancy-mediated diffusion between bcc Ti, Zr, and dilute Zr-Sn alloys and bcc Cr, Mo, and W. Our results indicate that strongly anharmonic vibrations promote both the vacancy concentration and the diffusive jump rate in bcc IVB metals and can explain their markedly faster diffusion compared to bcc VIB metals. Additionally, we provide an efficient approach to calculate diffusive jump rates according to the transition state theory (TST). The use of standard harmonic TST is impractical in bcc IIIB/IVB metals due to the existence of ill-defined harmonic phonons, and most studies use classical or *ab initio* molecular dynamics for direct simulation of diffusive jumps. Here, instead, we use a stochastically sampled temperature-dependent phonon analysis within the transition state theory to study diffusive jumps without the need of direct molecular dynamics simulations. We validate our first-principles diffusion coefficient predictions with available experimental measurements and explain the underlying reasons for the promotion of diffusion in bcc IVB metals/alloys compared to bcc VIB metals.

DOI: 10.1103/PhysRevMaterials.6.023803

I. INTRODUCTION

Diffusion in crystalline solids determines the kinetics of many diffusion-controlled phenomena, e.g., phase transformation, precipitate growth and coarsening, and corrosion, and understanding it is basic to predicting new materials with desired physical and mechanical properties. Diffusion in bcc solids is generally faster than close-packed phases of fcc and hcp due to their more open structure. However, within the bcc metals and their alloys, there are major differences in diffusion coefficient values. Specifically, self- and solute diffusion is orders of magnitude faster in bcc phases of IIIB-IVB metals compared to VB-VIB metals [1–10]. For example, self-diffusion in bcc Ti is $10^5 - 10^7$ times higher than bcc Cr despite similar mass and common lattice structure [3]. The underlying reason for this strikingly faster diffusion is still not fully understood. Specifically, the effect of strong anharmonic phonons on diffusion is understudied, considering that there is a fundamental difference between the nature of vibrations of bcc IIIB-IVB metals and VB-VIB metals. The bcc phase of the former group (IIIB-IVB metals and alloys) is only stable when it reaches high enough temperatures and experiences strongly anharmonic vibrations, i.e,, it is dynamically stabilized [11–16] as opposed to the bcc phase in the latter group (VB-VIB metals), which is stable at all temperatures. This dynamical stabilization despite the lattice instability implies that the Hamiltonian anharmonicity is so strong that it creates multiple local minima around a high-symmetry maximum. The system is stabilized by hopping among these local minima at elevated temperatures, as shown in our earlier studies of thermodynamic stability of bcc Ti and ordered bcc NiTi compounds [14,17]. Aside from existing gaps in understanding the effect of phonon anharmonicity on diffusion, application of the harmonic transition state theory (TST) becomes impossible due to the existence of ill-defined harmonic phonons, i.e., phonons with imaginary frequencies or negative thermal energy, in dynamically stabilized phases [18–20].

Several studies have investigated the underlying reasons for the so-called anomalously fast diffusion in bcc IIIB-IVB metals and alloys, which we classify into three groups. The first group has explained the enhanced diffusion by mixed vacancy mechanisms, the appreciable contribution of divacancy or self-interstitial jumps to the vacancy mechanism, especially near the melting point [1,5,21–24]. For example, Vogl *et al.* obtained two distinct jump frequencies for Co in bcc Zr from their quasielastic neutron scattering and speculated that jumps between interstitial sites might be the reason for the fast diffusion of Co [5]. Recently, Smirnov has observed formation of self-interstitial defects in a classical molecular dynamics simulation based on a modified embedded atom method (MEAM) potential model for bcc Ti, showing that the self-interstitial jumps can contribute up to 10% to the high-temperature diffusivity but become negligible at low temperature ranges [24]. Other EAM-potential molecular dynamics (MD) studies consistently predicted the formation of self-interstitial in bcc Ti and Zr at high temperatures [25,26]. According to these studies, self-interstitial jump contribution can explain the upward curvature of the Arrhenius plot for diffusion coefficients in bcc Ti and Zr at high temperature ranges, however, the markedly higher diffusivity compared to bcc VB-VIB, such as Cr or W, cannot be understood. Multiple isotope effect measurements and neutron scattering studies in

*Corresponding author: sarakad@uic.edu

bcc IIIB-IVB metals confirmed that the vacancy mechanism is the predominant diffusion mechanism [6–8,27–29], precluding explanations based on major contributions from other intrinsic defects, even at temperatures close to the melting point [29]. This led to the second group of studies, which related the anomalously fast and non-Arrhenius diffusion to soft phonon modes or to fluctuation of bcc IIIB-IVB metals between metastable ω-phase embryos. Sanchez and de Fontaine proposed a model which correlates the diffusivity in bcc Zr to the formation of the metastable ω phase and uses the formation free energy of the ω embryo as the diffusion activation energy [30–32]. Herzig and Köhler explained the anomalously fast diffusion and strong non-Arrhenius behavior in bcc IIIB-IVB metals according to the characteristic soft phonon mode LA $\frac{2}{3}\langle 111\rangle$, and provided a semiempirical relation between diffusive migration enthalpy and the square of the soft phonon frequency [3,33,34]. Kadkhodaei and Davariashtiyani illustrated that including the anharmonic phonon effects obtained from *ab initio* molecular dynamics to describe the activation energy and the effective frequency for a vacancy-mediated diffusive jump in bcc Ti and Zr can successfully reproduce the experimentally reported anomalous high diffusion coefficients [35]. The third group of studies related the enhanced diffusion to concerted motion of atoms or collective diffusion mechanisms [36,37]. Sangiovanni *et al.* observed a highly concerted string-like atomic motion in an *ab initio* molecular dynamics simulation in bcc Ti at 1800 K [36]. They predicted the diffusion coefficient of bcc Ti by accounting for both vacancy diffusivity and concerted atomic motion diffusivity obtained form MEAM-potential MD simulations, showing that the concerted motion diffusivity becomes non-negligible close to the melting point and can describe the non-Arrhenius curvature. Recently, MEAM-potential MD simulations in bcc and fcc metals demonstrated that vacancy-interstitial pairs form via a stringlike atomic motion along close-packed directions, which becomes particularly prevalent in bcc crystal structures, including Ti, Zr, Ta, and Nb [37]. According to these simulations, concentration of vacancy-interstitial pairs in bcc Zr, Ta, and Nb are in the same order, with bcc Ti showing exceptionally higher concentration and a strong deviation from the Arrhenius behavior at low temperature ranges. This study has linked the stringlike atomic motion to vacancy-interstitial pair formation, both observed separately in previous MEAM MD simulations [24,36]. Despite these studies, a systematic comparison of diffusion parameters between normal bcc metals of VB-VIB and anomalous bcc metals of IIIB-IVB is still lacking.

The contribution of this paper is twofold: First, we elucidate the underlying reason for the so-called anomalously faster diffusion in bcc IVB metals/alloys with a focus on the role of strongly anharmonic vibrations. We present a detailed comparison of diffusion parameters between mechanically stable bcc VIB metals and mechanically unstable but dynamically stabilized bcc IVB metals, including first-principle-calculated activation energies and effective vibration frequencies along the diffusive jump direction. We explain the role of strongly anharmonic vibrations in promoting diffusive jumps. Second, we provide an efficient approach to calculate the diffusion coefficient of bcc IVB metals without the need of any direct simulation of diffusive jumps. We employ temperature-dependent phonon analysis within the TST to predict diffusive jump frequencies, where the temperature-dependent phonons are obtained based on a stochastic sampling of vibrations, eliminating any molecular dynamics simulation for sampling the vibrations or diffusive jumps.

The content of this paper is arranged in the following manner: In Sec. II, we describe the methods used for temperature-dependent phonon analysis and density functional theory (DFT) calculations to predict the diffusion coefficient. In Sec. III, we illustrate the calculated diffusion parameters for bcc Cr, Mo, and W (as examples of mechanically stable or so-called normal bcc metals) versus bcc Ti, Zr, and Zr-0.46at.%Sn (as examples of dynamically stabilized or so-called anomalous bcc metals). In Sec. IV, we interpret the differences in diffusion parameters between normal and anomalous bcc systems in light of anharmonic lattice vibrations. Additionally, we discuss the findings of this paper in comparison to existing studies in the literature.

II. METHOD

We obtain the macroscopic diffusion coefficient, D, of self-diffusion or solute diffusion by a monovacancy mechanism in a bcc lattice according to the microscopic parameters in the following equation:

$$D = C_v d^2 \Gamma, \tag{1}$$

where d is the vacancy (or atom) jump distance, C_v is the equilibrium concentration of vacancy or vacancy-solute pair, and Γ is the successful vacancy jump rate [20]. Vacancy jump distance in bcc is equal to the nearest-neighbor distance or $\frac{\sqrt{3}}{2}a_0$, where a_0 is the lattice constant. The vacancy or vacancy-solute pair concentration at temperature T is given by $C_v = \exp(\frac{\Delta S_f}{k_B})\exp(-\frac{\Delta H_f}{k_B T})$, where ΔH_f and ΔS_f are the formation enthalpy and entropy of vacancy or vacancy-solute pairs, respectively, and k_B is the Boltzmann constant. The vacancy jump rate Γ is obtained from the migration enthalpy ΔH_m and the effective vibration frequency along the migration path ν^* by $\Gamma = \nu^* \exp(\frac{-\Delta H_m}{k_B T})$. According to the TST, the effective vibration frequency, ν^*, is the ratio of the product of normal vibration frequencies (or harmonic phonon frequencies) of the initial state of atomic migration, ν_i, to that of the nonimaginary normal frequencies of the transition state, ν'_j, i.e., $\nu^* = \frac{\prod_{i=1}^{3N-3}\nu_i}{\prod_{j=1}^{3N-4}\nu'_j}$ [19].

We calculate the microscopic parameters of diffusion, including ΔH_f, ΔS_f, ΔH_m, and ν^*, in different ways for the normal and anomalous bcc systems: For normal bcc metals, including Cr, Mo, and W, we employ the standard approach [20] based on DFT total energy calculations, the climbing image nudged elastic band (c-NEB) method for locating the transition state [38], and the frozen phonon method for harmonic phonon analysis [39]. For anomalous bcc metals, we provide an approach that uses a stochastic sampling of the canonical ensemble to describe vacancy formation enthalpy and entropy, vacancy migration enthalpy, and effective vibration frequency. Details of each approach are explained in the following.

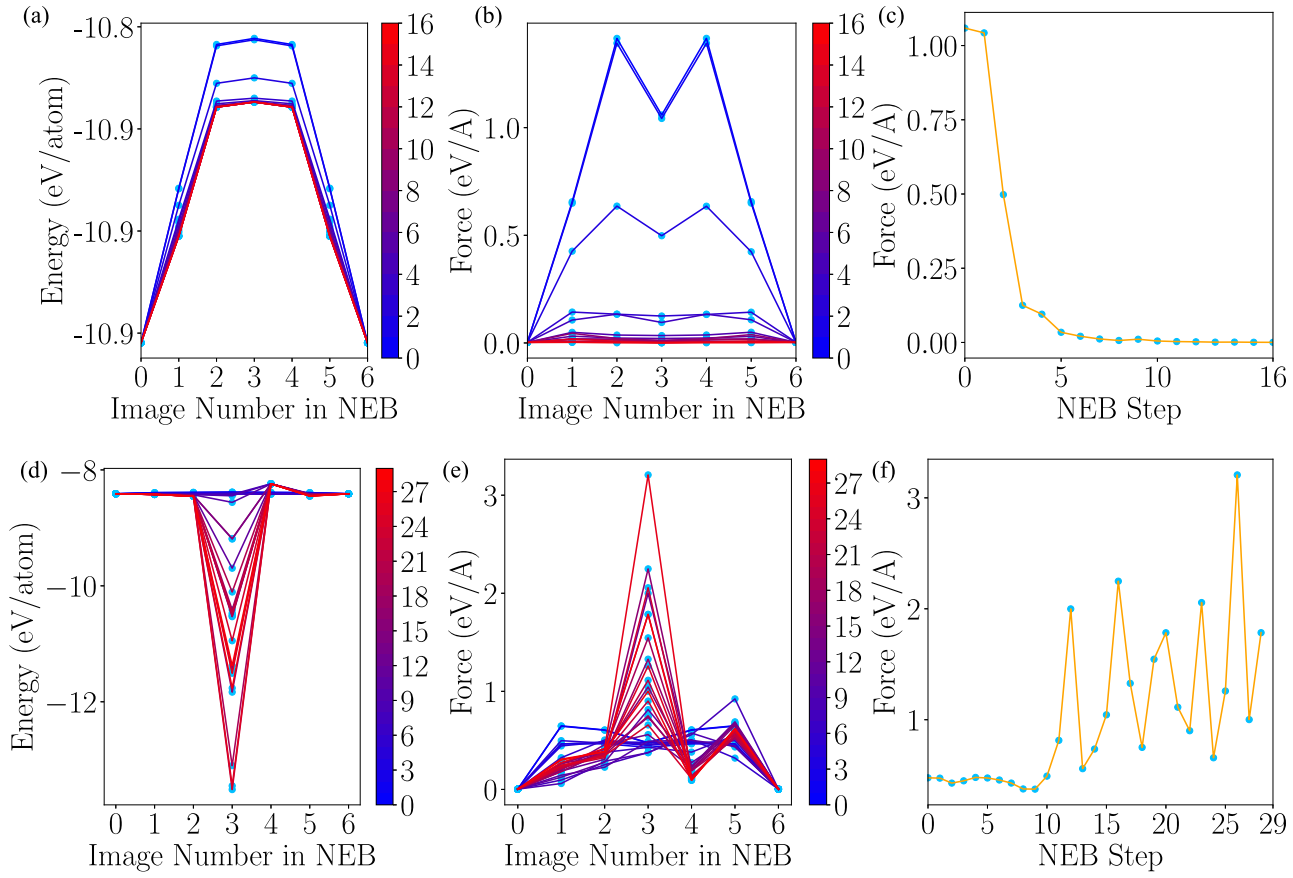

FIG. 1. The evolution of the NEB to optimize the initial energy profile to the final minimum energy path for bcc Mo versus bcc Zr. The initial band consists of five images interpolated along the $\frac{1}{2}[111]$ nearest-neighbor vacancy jump (or diffusive jump) direction. (a), (d) The energy evolution on each image throughout the NEB optimization for bcc Mo and bcc Zr, respectively. (b), (e) The force evolution on each image for bcc Mo and bcc Zr, respectively. (c), (f) The maximum force on the climbing image at each NEB iteration for bcc Mo and bcc Zr, respectively

For Cr, Mo, and W, the equilibrium lattice constant, a_0, is calculated by finding the minimum DFT energy for five different volumes incremented by 2% lattice constant expansion. The vacancy formation enthalpy is calculated as the difference of DFT total energies of the defected and bulk systems, $E(N-1)$ and $E(N)$, according to $\Delta H_v = E(N-1) - \frac{N-1}{N}E(N)$, for a system of N atoms. The vacancy formation entropy is calculated similarly according to $\Delta S_v = S^{\text{vib}}(N-1) - \frac{N-1}{N}S^{\text{vib}}(N)$. The vibration entropy, S^{vib}, is calculated from to the harmonic phonon density of states according to the Supplemental Material Eq. (4) [40]. The harmonic phonon density of states are calculated from the temperature-independent force-constant using the frozen phonon approach as implemented in the PHONOPY package [39]. We use the climbing image NEB method based on DFT forces to obtain the minimum energy path and the saddle point (or the transition state of diffusion) [38]. Figures 1(a)–1(c) shows the NEB optimization for bcc Mo; for example. Supplemental Material Fig. 1 [40] shows the NEB optimization for other bcc metals. Subsequent to the transition sate optimization, we compute the migration enthalpy, ΔH_m, as the difference between the DFT total energies of the initial atomic configuration and the activated transition state, $\Delta H_m = E^{\text{activated}}(N-1) - E^{\text{initial}}(N-1)$. The effective vibration frequency ν^* is obtained by calculating the normal vibration modes for the initial and the saddle point atomic configurations. For dynamically stabilized bcc Ti, Zr, and Zr-0.46at.%Sn, we provide an approach that can effectively include the temperature-dependent anharmonic vibrations into the diffusion calculation. Due to the mechanical instability of the bcc lattice in these systems, the formation or migration enthalpy cannot be approximated by the total energy difference of bulk and defected or activated supercells, considering that the DFT energy corresponds to the free energy at absolute zero temperature, where these systems do not even exist. An additional difficulty arising from the lattice instability is the divergence of saddle point search schemes based on DFT forces. As compared in Figs. 1(a) and 1(b) and 1(d) and 1(e), the NEB method can optimize an initial energy profile along the $\frac{1}{2}[111]$ nearest-neighbor vacancy jump direction to the final minimum energy path and therefore can locate the transition state in bcc Mo, while it fails to locate the transition state in bcc Zr based on DFT forces. Figure 1(f) shows that the maximum force on the climbing image diverges for bcc Zr (see Supplemental Material Fig. 1 for bcc Ti [40]), whereas Fig. 1(c) shows the convergence of the maximum force on the climbing image in bcc Mo (see Supplemental Material Fig. 1 for bcc Cr and W [40]). To overcome these challenge, we generate three different canonical ensembles for each anomalous bcc metal. One for the defect-free or bulk supercell, one for the defected super-

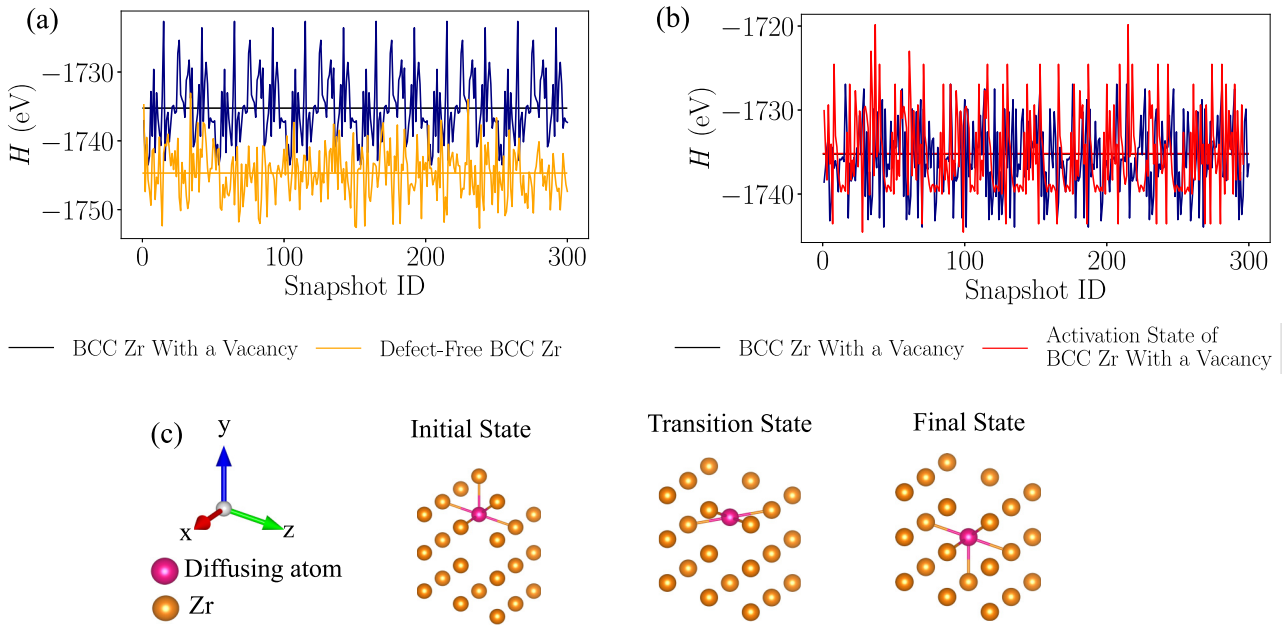

FIG. 2. Stochastic sampling of the canonical ensemble for dynamically stabilized bcc systems. (a) Enthalpy at 1400 K for all the stochastic snapshots of the defect-free bcc Zr (blue) and defected bcc Zr with a monovacancy (orange). (b) Enthalpy at 1400 K for all the stochastic snapshots of the defected bcc Zr with a monovacancy (blue) and the activated defected bcc Zr with the diffusing atom halfway between neighboring bcc lattice sites (orange). The horizontal lines represent averages over all the snapshots. (c) Static atomic configurations, i.e., atoms sitting at the lattice sites without any momentum, around the vacancy for the initial, transition (or activated), and final states of diffusion. Diffusing Zr atom is shown by a different color. The static transition state is approximated by an atomic configuration where the diffusing atom sits between two vacant neighboring lattice sites.

cell (including a monovacany or a vacancy-solute pair) and one for the activated transition state. The canonical ensembles are generated using the Maxwell-Boltzmann statistics according to the stochastic temperature-dependent effective potential (or s-TDEP) method [41–45]. The atomic positions and velocities are generated using the harmonic normal-mode transformation, as detailed in Supplemental Material Note 1 and Supplemental Material Eqs. (2) and (3) [40], resulting in uncorrelated excited states (or snapshots) for each ensemble. Unlike the bulk and equilibrium defected states, the activated transition state is a semiequilibrium state, for which the canonical ensemble is obtained by generating multiple atomic snapshots with stochastic positions and velocities, except for the diffusing atom which has a fixed position at halfway along the $\frac{1}{2}[111]$ diffusive jump direction but has a stochastic velocity. This construct assumes that the saddle point on an effective temperature-dependent energy surface coincides with the atomic configuration with diffusing atom at $\frac{1}{4}[111]$ lattice point [see Fig. 2(c)]. We use DFT to calculate atomic forces, total energy, and pressure for each stochastic snapshot in the ensembles. For the canonical ensemble at 1400 K, we calculate the Helmholtz free energy from the stochastic snapshots (as described below) for six different volumes incremented by $0.02a_0$ and select the volume with the lowest free energy as the equilibrium volume for the canonical ensemble (same method used in Ref. [45]). We use the same volume for supercells at other temperatures. The enthalpy values are obtained by averaging the total energy (sum of the ion-electron and the kinetic energies), $\langle U\rangle$, and the pressure-volume term, $\langle p\rangle V$, over the snapshots for each ensemble according to $H = \langle U\rangle + \langle p\rangle V$, as shown in Fig. 2. The vacancy formation and migration enthalpy values are then obtained according to $\Delta H_v = H(N-1) - \frac{N-1}{N}H(N)$ and $\Delta H_m = H^{\text{activated}}(N-1) - H^{\text{initial}}(N-1)$, respectively. We confirmed that the average total energy obtained from the stochastic snapshots agrees well with the average total energy obtained from a canonical *ab initio* molecular dynamics simulation. More details are provided in Supplemental Material Fig. 2 [40]. For all the bcc metals, we incorporate the intrinsic surface correction terms to the vacancy formation and migration enthalpy values as shown in Supplemental Material Table 1 [40]. These correction terms are calculated based on the method proposed in Ref. [46] and compensate for the underestimation of DFT generalized gradient approximations (GGA) in calculating the intrinsic surface energy that is formed around a vacancy.

For bcc Ti, Zr, and Zr-Sn systems, phonons at elevated temperatures are calculated from the effective (or converged) temperature-dependent second-order force-constant according to the TDEP method [41–43]. The displacements and forces on stochastic atomic snapshots are recorded, and the force constant is obtained via a least-squares fitting of an effective harmonic potential model of Supplemental Material Eq. (1) [40] to the displacement-force data set. The force constant is converged through a self-consistent process with respect to the number of snapshots and iterations. At each temperature, 50 stochastic snapshots are generated initially using a model force-constant that emulates the Debye temperature (as explained in Ref. [44]). The calculated force constant at each iteration is then used to generate a new set of stochastic snapshots for the next iteration (see Supplemental Material Eqs. (2) and (3) [40]). The number of snapshots is increased as the iteration continues to ensure

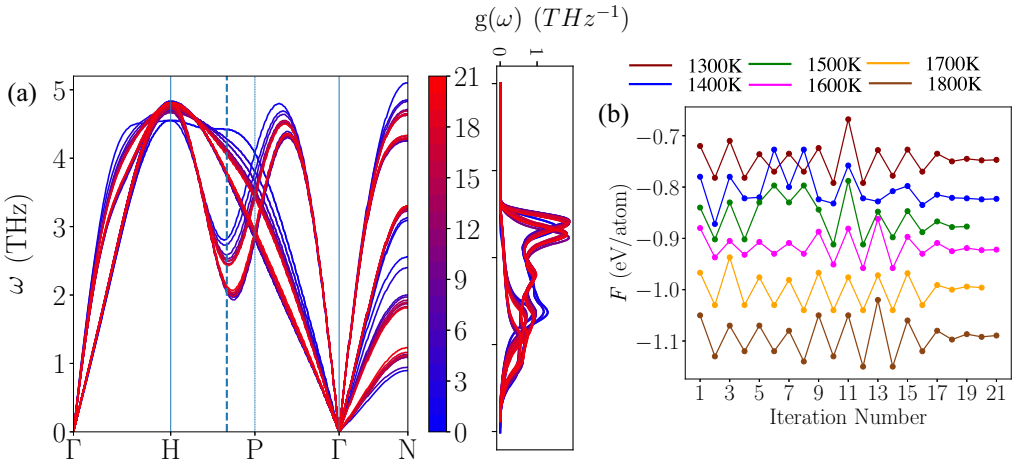

FIG. 3. Iterative temperature-dependent phonon analysis for the defect-free bcc Zr. (a) Phonon dispersion and density of states evolution during the s-TDEP iterations at 1400 K. (b) Phonon free energy evolution during the s-TDEP iterations for bcc Zr at different temperatures.

the convergence of the phonon free energy, with the last iteration consisting of 300 stochastic snapshots. Throughout the s-TDEP iterations, the phonon free energy is calculated using Supplemental Material Eq. (4) [40]. Convergence is achieved when the phonon free energy difference between consecutive iterations falls below 3 meV per atom. Figure 3 shows the evolution of the phonon dispersion, phonon density of states, and phonon free energy through the s-TDEP iterations for the defect-free bcc Zr. The vacancy formation entropy, ΔS_f, is calculated based on the difference of the vibration entropy for the defected and bulk systems, each calculated from the temperature-dependent phonon density of states (e.g., see Fig. 4 and Supplemental Material Fig. 3 [40]) according to Supplemental Material Eq. (4) [40]. The effective prefactor frequency along the diffusive jump direction, ν^*, is approximated as the temperature-dependent phonon frequency at $\frac{2}{3}$ along the L$\langle\xi\xi\xi\rangle$ or Γ-H-P branch for the defected system. The atomic distortion for this phonon mode coincides with the vacancy jump direction for the bcc phase. Figure 4 shows the temperature-dependent phonon dispersion and density of states calculated at 1400 K for defected bcc Zr and Zr-0.46at.%Sn. For defected systems, ν^* or phonon frequency at $\frac{2}{3}$L$\langle 111\rangle$ is obtained from the unfolded phonon dispersion. For phonon band unfolding, we use the method of Ref. [47] by imposing the bcc unit cell symmetry path of Γ, H, P, Γ, and N to the defected supercell (see Fig. 4).

Details of the DFT and NEB calculations are as follows: For Cr, Mo, and W, a $5 \times 5 \times 5$ supercell of conventional bcc unit cell with 250 atoms is used for the bulk system. For bcc Ti, Zr, and Zr-Sn, a $6 \times 6 \times 6$ supercell containing 216

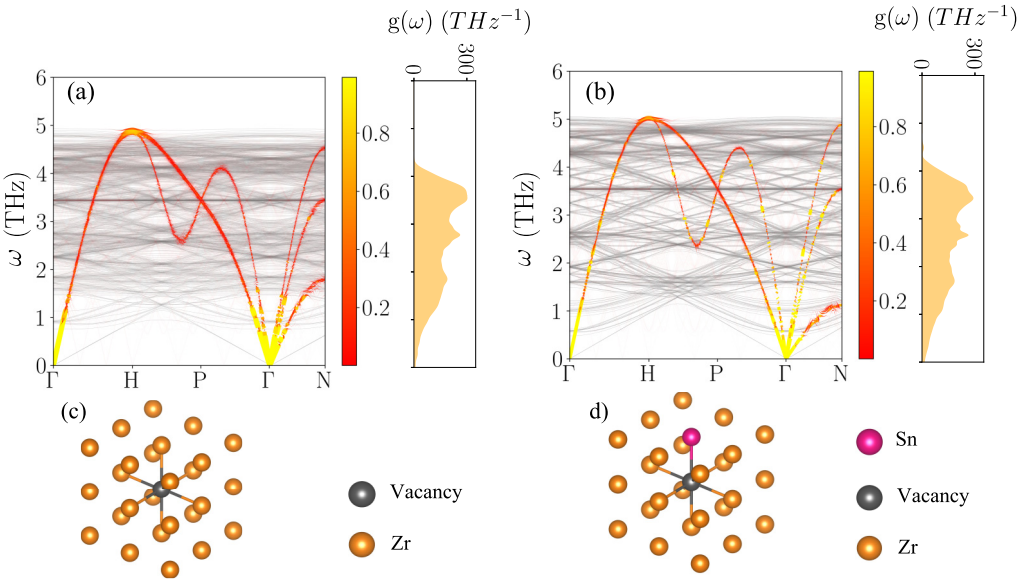

FIG. 4. The temperature-dependent phonon dispersion and density of states for (a) the defected bcc Zr at 1400 K and (b) the defected bcc Zr-0.46at.%Sn at 1400 K. The folded dispersion is shown by gray and the unfolded dispersion is shown by a color map that indicates the spectral function of the unfolding. The atomic configuration of (c) the defected bcc Zr around the isolated vacancy and (d) the defected bcc Zr-0.46at.%Sn around the vacancy-solute pair.

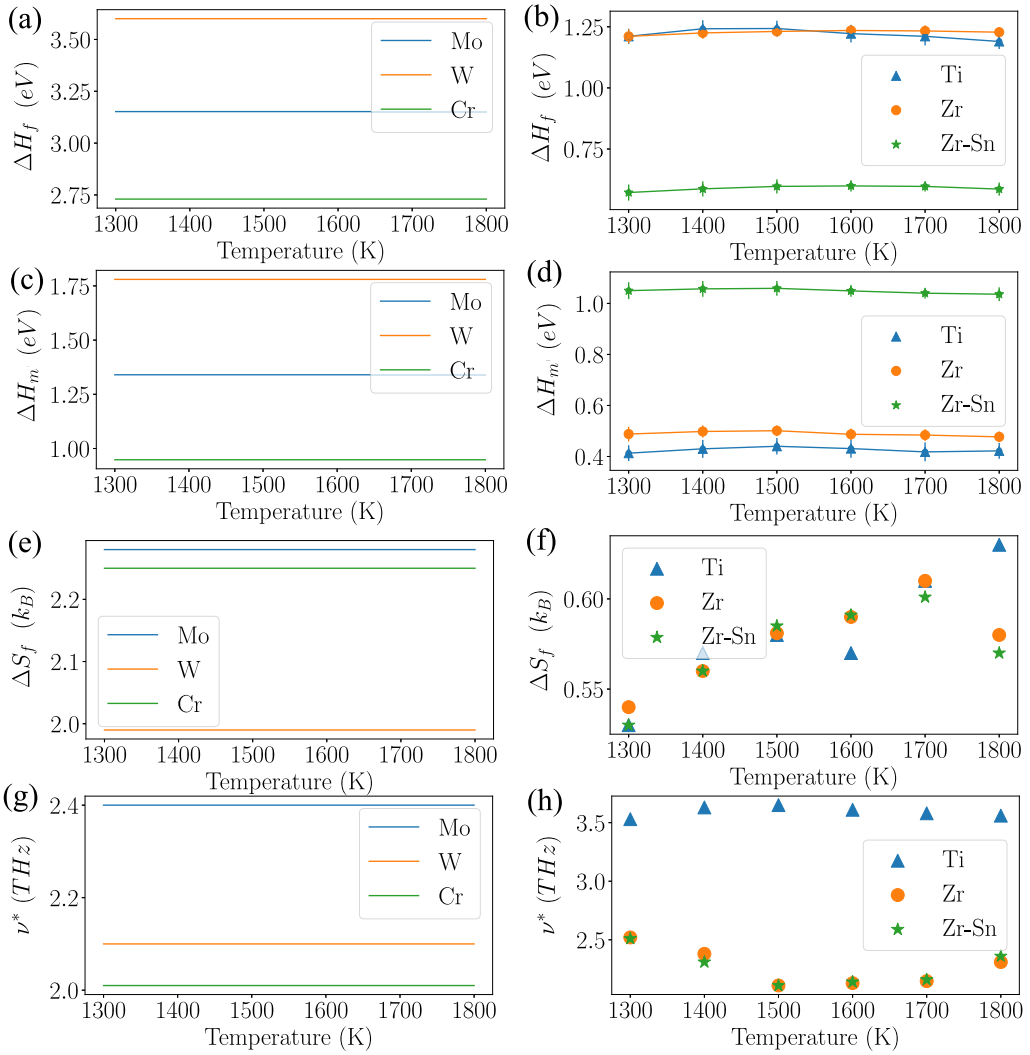

FIG. 5. Microscopic diffusion parameters for mechanically stable bcc metals (left column) and dynamically stabilized bcc systems (right column). (a), (b) Vacancy formation enthalpy, ΔH_f. (c), (d) Vacancy migration enthalpy, ΔH_m. (e), (f) Vacancy formation entropy, ΔS_f. (g), (i) Effective prefactor frequency, ν^*. Error bars indicate the standard deviation of the stochastic snapshots at each temperature (for each canonical ensemble).

atoms is used for the bulk state and the defected supercell consists of 215 atoms. We use the projector-augmented-wave method as implemented in the highly efficient VIENNA AB INITIO SIMULATION PACKAGE [48–51]. For Cr, Mo, and W, we use a Monkhorst-Pack k-point mesh of $3 \times 3 \times 3$ and an energy cutoff of 350 and 320 and 300, respectively, within the Perdew-Burke-Ernzerhof (PBE) exchange-correlation functional. For Zr, Ti, and Zr-Sn, a $1 \times 1 \times 1$ Monkhorst-Pack k-point grid, and a plane-wave energy cutoff of 350 eV within the PBE exchange-correlation functional [52]. We use the spring constant of 5.0 eV/Å^2 for all the NEB calculations and convergence is assumed when the maximum atomic force on all the images falls below 0.01 eV/Å.

III. RESULTS

We calculate the individual microscopic diffusion parameters, namely, the vacancy formation enthalpy, ΔH_f, vacancy migration enthalpy, ΔH_m, vacancy formation entropy, ΔS_f, and effective prefactor frequency, ν^*, for the mechanically stable versus dynamically stabilized bcc systems as explained in Sec. II. As shown in Fig. 5, diffusion parameters for the mechanically stable bcc metals (Cr, Mo, and W) are temperature independent because the formation and migration enthalpies are calculated from DFT total energies of bulk and defected atomic configurations and formation entropy and effective prefactor frequency are calculated from the harmonic phonon density of states and harmonic TST. On the other hand, diffusion parameters for dynamically stabilized bcc Ti, Zr, and Zr-0.46at.%Sn show temperature dependence as expected when calculated from stochastically sampled canonical ensembles and temperature-dependent phonon analysis.

The formation and migration enthalpies for dynamically stabilized bcc phases are lower than their mechanically stable counterparts, as illustrated in Figs. 5(a)–5(d). For example, ΔH_f (or ΔH_m) is 2.73 eV (or 0.948 eV) for bcc Cr compared to 1.242 eV (or 0.43 eV) at 1400 K for bcc Ti with a similar atomic size or it is 3.152 eV (or 1.34 eV) for bcc Mo compared to 1.225 eV (or 0.498 eV) at 1400 K for bcc Zr (read from Table I). Among mechanically stable bcc metals, formation

TABLE I. Diffusion Parameters of bcc Mo, W, Cr, Zr, Ti, and Zr-Sn. The following superscripts are used: $**$: Calculated value at 1400 K in this paper,.*a*: DFT simulation with AM05 functional [53]. *b*: DFT Simulation with PBE functional [54]. *c*: DFT Simulation with PBE functional [55]. *d*: Experimental value from modulation measurements of specific heat [56]. *f*: From static lattice Green's function, which is directly calculated from experimental phonon density of states [57]. *g*: From force-constants fitted to the measured phonon dispersion curves [57]. *h*: Values at 0 K from quenched molecular dynamics [23].

		Mo	W	Cr	Ti	Zr	Zr-Sn(0.46at%)
a_0 (Å)	This paper	3.135	3.185	2.84	3.28**	3.59**	3.59**
	Reference	3.134[a]	3.186[b]	2.84[c]	3.25[c]		
ΔH_f (eV)	This paper	3.152	3.6	2.73	1.242**	1.225**	0.578**
	Reference	3.1[a]-3.07[c]	3.51[c]	3.05[c]	1.55[d]	1.75[d]-1.53[h]	
ΔS_f (k_B)	This paper	2.28	1.99	2.25	0.57**	0.56**	0.56**
	Reference	2.3[a]	1.8[g]	1.8[g]	2.4[g](1293 K)	2.58[g](1483 K) - 0.5[h]	
ΔH_m (eV)	This paper	1.34	1.78	0.948	0.43**	0.498**	1.057**
	Reference	1.3[a]	1.78[b]	0.95[c]	0.31[f](1293 K)	0.324[f](1483 K)-0.32[h]	
ν^* (THz)	This paper	2.4	2.1	2.01	3.63**	2.38**	2.31**
C_v	This paper	6.90E-11**	8.02E-13**	1.409E-09**	5.97E-05**	6.81E-05**	1.34E-2**
$\Gamma(Hz)$	This paper	3.6E+07**	8.21E+05**	1.15E+09**	1.02E+11**	3.5E+10**	3.61E+08**

and migration enthalpies increase by atomic size, lowest for Cr and largest for W [see Figs. 5(a), 5(c) and 6]. However, in between dynamically stabilized systems, the atomic size has a reduced significance. As shown in Figs. 5(b) and 5(d), the formation enthalpy values for bcc Ti and Zr are almost the same and the migration enthalpy for Ti is only slightly higher than Zr. However, ΔH_f for Zr-Sn is largely decreased compared to Ti and Zr while ΔH_m exhibits a large increase. This is because of the large binding energy between tin solute and vacancy (1.225 eV–0.56 eV = 0.66 eV at 1400 K, read from Table I). The attractive nature of the binding decreases the formation energy and subsequently increases the vacancy-solute concentration (as reported in Table I). On the other hand, the attractive binding energy resists the solute-vacancy exchange or migration and increases ΔH_m compared to the monovacancy migration in Zr or Ti. The relative lower activation enthalpies (formation + migration) of bcc Ti, Zr, and Zr-Sn is due to the dynamically stabilized nature of these phases. In fact, they reside on high-energy regions of the potential energy surface as opposed to a deep well (or low-energy local minimum) in mechanically stable bcc metals. This implies a flat energy profile along the migration pathway (see Fig. 6), which relatively reduces ΔH_m and a shallow well of residence which relatively reduces ΔH_f. The shallow nature of the residing well implies the existence of soft bonds or phonons with lower frequencies for dynamically stabilized bcc phases, leading to ΔS_f of about three to four times lower than mechanically stable bcc systems with the more pronounced vacancy-induced softening effect [see Figs. 5(e) and 5(f)]. ν^* for dynamically stabilized bcc metals is only slightly higher than their mechanically stable counterparts [see Figs. 5(g), 5(h) and Table I].

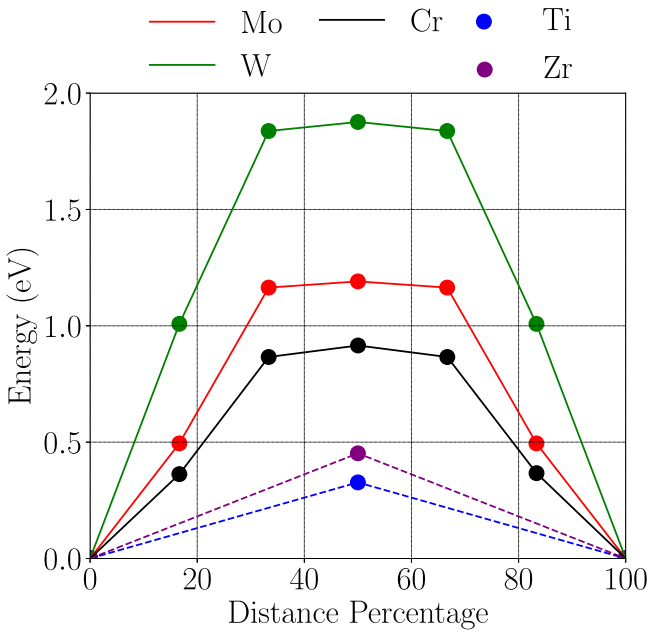

FIG. 6. DFT energy versus distance percentage along the vacancy diffusion pathway. For Mo, W, and Cr, the energy profile is optimized using the c-NEB. For Ti and Zr, the represented energy barrier is the DFT energy between the static atomic configurations of the initial and transition state, approximated by fixing the diffusing atom at the $\frac{1}{4}$[111] position. The calculated migration barrier for bcc Ti and Zr are calculated from average enthalpies over canonical stochastic snapshots instead of static configurations (see Fig. 2).

In Table I, we compare the calculated diffusion parameters with available values in the literature. For bcc Cr, Mo, and W, our predictions of a_0, ΔH_f, ΔH_m, and ΔS_f are in perfect agreement with other DFT predictions [53–55], with the only exception of ΔH_f for bcc Cr being lower than the DFT study in Ref. [55]. For bcc Ti and Zr, DFT data are few due to computational difficulties associated with the lattice instability. Therefore, we compare our predictions with available data that are directly measured or calculated from other measurements (more details are provided in Table I). Our ΔH_f for bcc Ti and Zr are relatively lower than the formation enthalpies evaluated from the nonlinear increase in specific heat via modulation measurements in Ref. [56] but show the same trend between Ti and Zr. Our ΔH_m values for bcc Ti and Zr are slightly higher than the values evaluated from measured phonon density of states in Ref. [57] but ΔH_m for bcc Zr closely match the prediction from a quench molecular dynamics study [23]. Our ΔS_f for bcc Ti and Zr

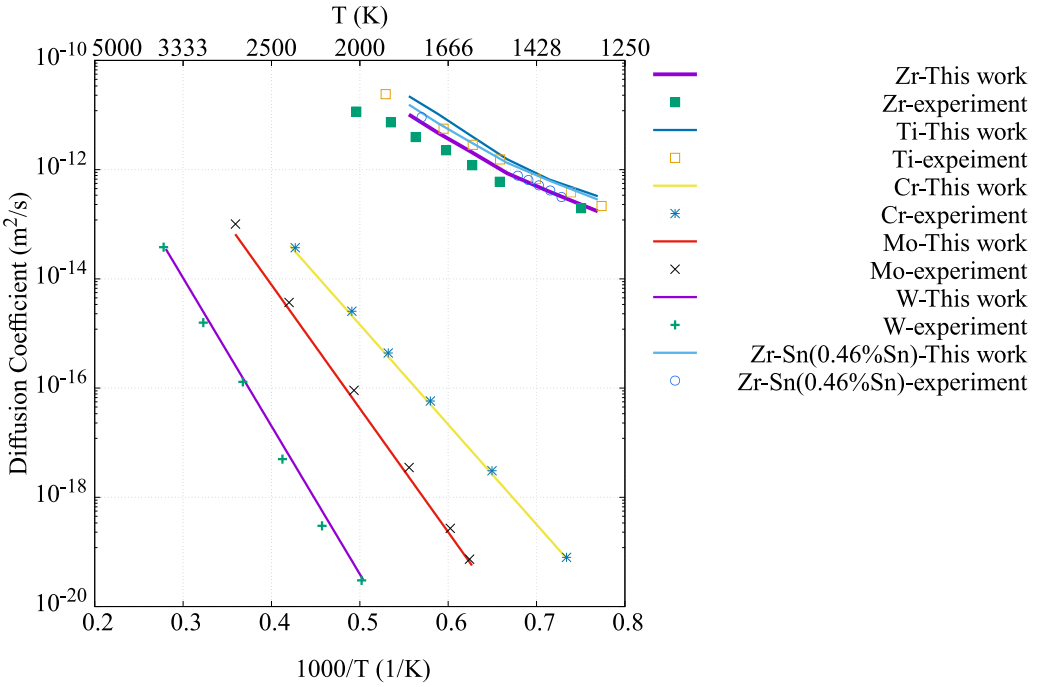

FIG. 7. Self- and solute diffusion coefficients versus temperature in bcc IVB and VIB metals. The predictions in this paper are from first-principles calculations, compared against experimental measurements of Ref. [3] for pure systems and Ref. [58] for the Zr-Sn alloy.

are lower than the evaluations from Born-von Karman fits to the measured phonon dispersion curves [57] (see Table I), however, they closely match predictions from 0 K calculations of quenched molecular dynamic snapshots of Ref. [23], as reported in Table I. Our ΔS_f for bcc Cr and W, on the other hand, are in better agreement with values of Ref. [57]. The evaluated parameters of Ref. [57] only provides estimates and should not be considered as quantitative, especially in cases of strong anharmonictiy of phonons (see Sec. 6.3. in Ref. [57]).

In addition to microscopic diffusion parameters, we report the vacancy (or vacancy-tin pair) concentration and the successful vacancy jump rate, C_v and Γ, as defined in Sec. II. C_v and Γ for dynamically stabilized bcc systems are both orders of magnitude higher than their mechanically stable counterparts (see reported values at 1400 K in Table I). For example, C_v at 1400 K is 6.8E-05 for bcc Zr compared to 6.90E-11 for bcc Mo (almost 10^6 times higher) or 5.97E-05 for bcc Ti compared to 1.409E-09 for bcc Cr (more than 40 000 times higher). Similarly, Γ at 1400 K is 3.5E+10 Hz for bcc Zr compared to 3.6E+07 Hz for bcc Mo (around 850 times higher) or it is 1.02E+11 Hz for bcc Ti compared to 1.15E+09 Hz for bcc Cr (around 100 times higher). The markedly higher vacancy concentration and successful diffusive jump rate both contribute to the strikingly higher diffusivity in dynamically stabilized bcc phases compared to the mechanically stable ones (see Fig. 7). Among mechanically stable bcc phases, C_v exhibits a strong dependence on the atomic size, similar to ΔH_f as expected, with the highest vacancy concentration in Cr and lowest in W. Unlike mechanically stable bcc metals, C_v is less sensitive to atomic size in dynamically stabilized bcc systems, similar to the weak dependence of ΔH_f on atomic size in these phases.

Figure 7 shows the calculated diffusion coefficients from the diffusion parameters according to Eq. (1) for all bcc systems compared against available experimental values. Dynamically stabilized bcc systems, Ti, Zr, and Zr-Sn, show around $10^5 - 10^6$ times higher diffusion coefficients compared to mechanically stable bcc metals, Cr, Mo, and W. The markedly higher diffusivity is more pronounced at lower temperatures, as expected based on the Arrhenius *D-T* relation. Another remarkable difference is that diffusion coefficients of bcc Ti, Zr, and Zr-Sn only span over a narrow range ($10^{-11} - 10^{-13}$ m^2/s) while diffusivities of bcc Cr, Mo, and W span over a wider range ($10^{-14} - 10^{-20}$ m^2/s). This is because of the lower downward slope of the *D-T* curves in the former group arising from lower activation enthalpies. Among bcc Ti, Zr, and Zr-Sn, *D* values are very close, unlike bcc Cr, Mo, and W, where diffusivities are distinctly different with a strong dependence on the size of diffusing atom, lowest for W and highest for Cr. Among anomalous bcc systems, the order of self- or solute diffusion from high to low is Ti, Zr-Sn, Zr. The slightly higher diffusivity of Ti compared to Zr can be attributed to higher vacancy jump frequency (e.g., 3.34 times higher in Ti compared to Zr at 1400 K) while vacancy concentration of Ti and Zr are almost the same (compare values in Table I). The slight higher diffusivity of Zr-Sn compared to Zr, on the other hand, arises from the trade-off between the increased vacancy concentration in Zr-Sn (≈200 times higher than Zr at 1400 K) and the reduced vacancy jump frequency (≈0.01 times lower than Zr at 1400 K). This is because of the large attractive binding between tin solute and vacancy, which significantly favors vacancy-solute pair formation but

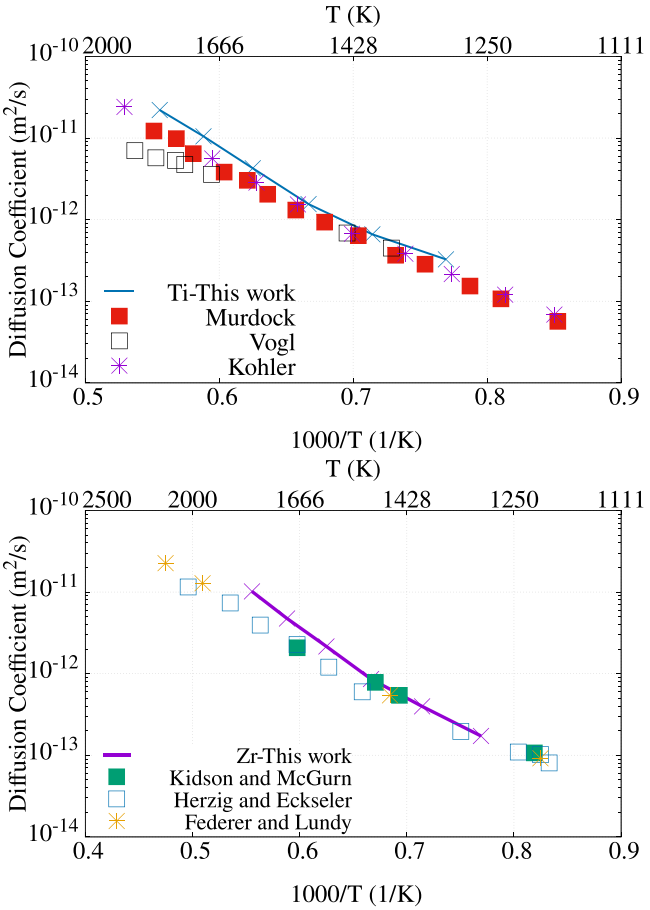

FIG. 8. Self-diffusion in bcc Ti (top) and bcc Zr (bottom) versus temperature. The references to experimental results are Murdock *et al.* [1], Vogl *et al.* [6], Köhler and Herzig [33], Kidson and McGurn [59], Herzig and Eckseler [60], and Federer and Lundy [61]

it increases the migration enthalpy. As shown in Fig. 7, our first-principles predictions of diffusion coefficient are in good agreement with experimental measurements [3,58]. For self-diffusion in bcc Ti and Zr, a more detailed comparison of our diffusivity predictions with several experimental measurements [1,6,33,59–61] is shown in Fig. 8. Our calculated diffusion coefficients agree well with all measured values and show a slight curvature in the Arrhenius plots. In Supplemental Material Figure 4 [40], we evaluate the dependence of the curvature of Arrhenius plots on the temperature-dependence of different diffusion parameters in bcc Ti and Zr.

IV. DISCUSSION

Our first-principles calculations indicate that the anomalously higher diffusivity in dynamically stabilized bcc phases stems from both the increased vacancy concentration and successful diffusive (or vacancy) jump rate. Both increases are a direct result of the strongly anharmonic nature of vibrations in these phases: (1) Monovacany formation is significantly promoted in these phases because of the nature of the free energy surface, which corresponds to a shallow well. In fact, the bcc lattice instability is so strong that it creates multiple local minima on the energy surface around the bcc structure associated with local lattice distortions, and the system is effectively residing on a high-energy shallow well by hopping among the local structural distortions. (2) Monovacany diffusive jump rate is significantly promoted due to the coincidental softening of restoring forces along the $\frac{1}{2}[111]$ diffusive jumps, a direct result of strong anharmonicity of phonons (or phonon softening) along this direction (compare the phonon dispersion curves for bcc Zr, Zr-Sn, and Ti with those for bcc Cr, Mo, W in Fig. 4 and Supplemental Material Fig. 5 [40]).

We incorporate the strongly anharmonic vibration effects in the description of diffusion parameters, which enable us to predict the individual parameters of vacancy concentration and vacancy jump rate. This elucidates the role of strong phonon anharmonicity in anomalously fast diffusion in terms of two separate effects: (1) an effective shallow well of residence and (2) directional lattice softening along [111], both arising from strong lattice anharmonicity. Interestingly, these two effects are also the underlying reason for the heterophase fluctuations in anomalous bcc systems, i.e., the vibration-induced fluctuations between bcc and ω, which is studied extensively in the literature [31,62]. The earlier model by Sanchez and de Fontaine has effectively intertwined these two effects by relating the heterophase fluctuation to the anomalous diffusion. They assumed that the formation free energy of the ω phase is the diffusive activation barrier [30] based on the fact that the softening in L $\frac{2}{3}\langle 111\rangle$ phonon mode is associated with the low-frequency large-amplitude vibration that results in heterophase fluctuations in the same direction as diffusive hops in the bcc lattice.

The good agreement of available experimental diffusion coefficients with our first-principles predictions based on the monovacancy jump mechanism supports the dominant role of monovacancy diffusion in bcc metals, consistent with earlier incoherent quasielastic neutron-scattering experiments [29]. Our calculations suggest that the contribution of other diffusion mechanisms to macroscopic diffusivity is secondary but can become important, especially at high temperatures. Based on the presented calculations, we speculate that the secondary diffusion mechanisms are necessary for a more accurate prediction of the observed non-Arrhenius curvature in anomalous bcc systems. The temperature dependence of activation enthalpy and the prefactor frequency only result in a small curvature in the Arrhenius plots. Secondary mechanisms of diffusion are extensively discussed in the literature, e.g., crowdionlike mechanism [23], interstitialcy mechansim [24], or stringlike collective mechanisms [36].

ACKNOWLEDGMENTS

We would like to thank Dr. O. Hellman for kindly sharing the TDEP software package with us. This work was supported by the US National Science Foundation Award No. DMR-1954621. We used the Extreme Science and Engineering Discovery Environment (XSEDE) through allocation No. TG-MAT200013, which is supported by National Science Foundation Grant No. ACI-1548562 resources [63].

[1] J. Murdock, T. Lundy, and E. Stansbury, Diffusion of Ti44 and V48 in titanium, Acta Metall. **12**, 1033 (1964).

[2] N. L. Peterson, Diffusion in the anomalous BCC metals, Comments Solid State Phys. **8**, 93 (1978).

[3] C. Herzig and U. Köhler, Anomalous Self-Diffusion in BCC IVB Metals and Alloys, in *Vacancies and Interstitials in Metals and Alloys*, Materials Science Forum Vol. 15 (Trans Tech Publications Ltd., Switzerland, 1987), pp. 301–322.

[4] C. Herzig, J. Neuhaus, K. Vieregge, and L. Manke, Fast Impurity Diffusion of Co and Fe in β-Zr and β-Zr-Alloys, in *Vacancies and Interstitials in Metals and Alloys*, Materials Science Forum Vol. 15 (Trans Tech Publications Ltd., Switzerland, 1987), pp. 481–486.

[5] G. Vogl, W. Miekeley, A. Heidemann, and W. Petry, Anomalously Fast Diffusion of Cobalt in β-Zirconium: Evidence for Two Different Jump Frequencies from Quasielastic Neutron Scattering, Phys. Rev. Lett. **53**, 934 (1984).

[6] G. Vogl, W. Petry, T. Flottmann, and A. Heiming, Direct determination of the self-diffusion mechanism in bcc β-titanium, Phys. Rev. B **39**, 5025 (1989).

[7] R. Peart and D. Tomlin, Diffusion of solute elements in beta-titanium, Acta Metall. **10**, 123 (1962).

[8] W. Petry, T. Flottmann, A. Heiming, J. Trampenau, M. Alba, and G. Vogl, Atomistic Study of Anomalous Self-Diffusion in bcc β-Titanium, Phys. Rev. Lett. **61**, 722 (1988).

[9] C. Herzig, U. Köhler, and S. V. Divinski, Tracer diffusion and mechanism of non-Arrhenius diffusion behavior of Zr and Nb in body-centered cubic Zr-Nb alloys, J. Appl. Phys. **85**, 8119 (1999).

[10] S. Nag, M. Sharma, and S. Yashonath, Understanding fast diffusion of solutes in solid solutions: A molecular dynamics study of solutes in body centered cubic solid, J. Chem. Phys. **153**, 244503 (2020).

[11] W. Petry, A. Heiming, J. Trampenau, M. Alba, and G. Vogl, Strong phonon softening in the BCC phase of titanium, Phys. B: Condens. Matter **156-157**, 56 (1989).

[12] K.-M. Ho, C. L. Fu, and B. N. Harmon, Vibrational frequencies via total-energy calculations. Applications to transition metals, Phys. Rev. B **29**, 1575 (1984).

[13] G. Grimvall, B. Magyari-Köpe, V. Ozoliņš, and K. A. Persson, Lattice instabilities in metallic elements, Rev. Mod. Phys. **84**, 945 (2012).

[14] S. Kadkhodaei, Q.-J. Hong, and A. van de Walle, Free energy calculation of mechanically unstable but dynamically stabilized bcc titanium, Phys. Rev. B **95**, 064101 (2017).

[15] K. Persson, M. Ekman, and V. Ozoliņš, Phonon instabilities in bcc Sc, Ti, La, and Hf, Phys. Rev. B **61**, 11221 (2000).

[16] Y. Y. Ye, Y. Chen, K. M. Ho, B. N. Harmon, and P. A. Lindgrd, Phonon-Phonon Coupling and the Stability of the High-Temperature bcc Phase of Zr, Phys. Rev. Lett. **58**, 1769 (1987).

[17] S. Kadkhodaei and A. van de Walle, First-principles calculations of thermal properties of the mechanically unstable phases of the PtTi and NiTi shape memory alloys, Acta Mater. **147**, 296 (2018).

[18] H. Eyring, The activated complex in chemical reactions, J. Chem. Phys. **3**, 107 (1935).

[19] G. H. Vineyard, Frequency factors and isotope effects in solid state rate processes, J. Phys. Chem. Solids **3**, 121 (1957).

[20] M. Mantina, Y. Wang, R. Arroyave, L. Q. Chen, Z. K. Liu, and C. Wolverton, First-Principles Calculation of Self-Diffusion Coefficients, Phys. Rev. Lett. **100**, 215901 (2008).

[21] J. Askill and G. B. Gibbs, Tracer diffusion in β-titanium, Phys. Status Solidi B **11**, 557 (1965).

[22] R. F. Peart and J. Askill, The mechanism of diffusion in b.c.c. transition metals, Phys. Status Solidi B **23**, 263 (1967).

[23] F. Willaime and C. Massobrio, A molecular dynamics study of zirconium based on an N-body potential: HCP/BCC phase transformation and diffusion mechanisms in the BCC-phase, MRS Online Proceedings Library **193**, 295 (1990).

[24] G. Smirnov, Non-Arrhenius diffusion in bcc titanium: Vacancy-interstitialcy model, Phys. Rev. B **102**, 184110 (2020).

[25] M. I. Mendelev and B. S. Bokstein, Molecular dynamics study of self-diffusion in Zr, Philos. Mag. **90**, 637 (2010).

[26] M. I. Mendelev, T. L. Underwood, and G. J. Ackland, Development of an interatomic potential for the simulation of defects, plasticity, and phase transformations in titanium, J. Chem. Phys. **145**, 154102 (2016).

[27] M. S. Jackson and D. Lazarus, Isotope effect for diffusion of tin in β-titanium, Phys. Rev. B **15**, 4644 (1977).

[28] L. Manke and C. Herzig, Diffusion und isotopieeffekt von silber in β-zirkon, Acta Metall. **30**, 2085 (1982).

[29] W. Petry, A. Heiming, J. Trampenau, and G. Vogl, On the diffusion mechanism in the bcc phase of the group 4 metals, in *Diffusion in Metals and Alloys*, Defect and Diffusion Forum Vol. 66 (Trans Tech Publications, Switzerland, 1991), pp. 157–174.

[30] J. M. Sanchez and D. de Fontaine, Model for Anomalous Self-Diffusion in Group-IV*B* Transition Metals, Phys. Rev. Lett. **35**, 227 (1975).

[31] J. Sanchez and D. De Fontaine, Anomalous diffusion in omega forming systems, Acta Metall. **26**, 1083 (1978).

[32] J. M. Sanchez, On the analysis of diffusion anomalies in Ti alloys, Philos. Mag. A **43**, 1407 (1981).

[33] U. Köhler and C. Herzig, On the anomalous self-diffusion in b.c.c. titanium, Phys. Status Solidi B **144**, 243 (1987).

[34] U. Köhler and C. Herzig, On the correlation between self-diffusion and the low-frequency LA $\frac{2}{3}\langle 111\rangle$ phonon mode in b.c.c. metals, Philos. Mag. A **58**, 769 (1988).

[35] S. Kadkhodaei and A. Davariashtiyani, Phonon-assisted diffusion in bcc phase of titanium and zirconium from first principles, Phys. Rev. Mater. **4**, 043802 (2020).

[36] D. G. Sangiovanni, J. Klarbring, D. Smirnova, N. V. Skripnyak, D. Gambino, M. Mrovec, S. I. Simak, and I. A. Abrikosov, Superioniclike Diffusion in an Elemental Crystal: bcc Titanium, Phys. Rev. Lett. **123**, 105501 (2019).

[37] E. Fransson and P. Erhart, Defects from phonons: Atomic transport by concerted motion in simple crystalline metals, Acta Mater. **196**, 770 (2020).

[38] G. Henkelman, B. P. Uberuaga, and H. Jónsson, A climbing image nudged elastic band method for finding saddle points and minimum energy paths, J. Chem. Phys. **113**, 9901 (2000).

[39] A. Togo and I. Tanaka, First principles phonon calculations in materials science, Scr. Mater. **108**, 1 (2015).

[40] See Supplemental Material at http://link.aps.org/supplemental/10.1103/PhysRevMaterials.6.023803 for a detailed presentation of the methods and results in the main text.

[41] O. Hellman, I. A. Abrikosov, and S. I. Simak, Lattice dynamics of anharmonic solids from first principles, Phys. Rev. B **84**, 180301(R) (2011).

[42] O. Hellman, P. Steneteg, I. A. Abrikosov, and S. I. Simak, Temperature dependent effective potential method for accurate free energy calculations of solids, Phys. Rev. B **87**, 104111 (2013).

[43] O. Hellman and I. A. Abrikosov, Temperature-dependent effective third-order interatomic force constants from first principles, Phys. Rev. B **88**, 144301 (2013).

[44] N. Shulumba, O. Hellman, and A. J. Minnich, Intrinsic localized mode and low thermal conductivity of PbSe, Phys. Rev. B **95**, 014302 (2017).

[45] F. C. Yang, O. Hellman, and B. Fultz, Temperature dependence of electron-phonon interactions in vanadium, Phys. Rev. B **101**, 094305 (2020).

[46] T. R. Mattsson and A. E. Mattsson, Calculating the vacancy formation energy in metals: Pt, Pd, and Mo, Phys. Rev. B **66**, 214110 (2002).

[47] Y. Ikeda, A. Carreras, A. Seko, A. Togo, and I. Tanaka, Mode decomposition based on crystallographic symmetry in the band-unfolding method, Phys. Rev. B **95**, 024305 (2017).

[48] P. E. Blöchl, Projector augmented-wave method, Phys. Rev. B **50**, 17953 (1994).

[49] G. Kresse and J. Hafner, *Ab initio* molecular dynamics for liquid metals, Phys. Rev. B **47**, 558 (1993).

[50] G. Kresse and J. Furthmüller, Efficiency of *ab-initio* total energy calculations for metals and semiconductors using a plane-wave basis set, Comput. Mater. Sci. **6**, 15 (1996).

[51] G. Kresse and J. Furthmüller, Efficient iterative schemes for *ab initio* total-energy calculations using a plane-wave basis set, Phys. Rev. B **54**, 11169 (1996).

[52] M. Ernzerhof and G. E. Scuseria, Assessment of the Perdew-Burke-Ernzerhof exchange-correlation functional, J. Chem. Phys. **110**, 5029 (1999).

[53] T. R. Mattsson, N. Sandberg, R. Armiento, and A. E. Mattsson, Quantifying the anomalous self-diffusion in molybdenum with first-principles simulations, Phys. Rev. B **80**, 224104 (2009).

[54] Y. Oda, A. M. Ito, A. Takayama, and H. Nakamura, First-principles study on migration of vacancy in tungsten, Plasma Fusion Res. **9**, 3401117 (2014).

[55] B. Medasani, M. Haranczyk, A. Canning, and M. Asta, Vacancy formation energies in metals: A comparison of MetaGGA with LDA and GGA exchange-correlation functionals, Comput. Mater. Sci. **101**, 96 (2015).

[56] Y. Kraftmakher, Equilibrium vacancies and thermophysical properties of metals, Phys. Rep. **299**, 79 (1998).

[57] H. R. Schober, W. Petry, and J. Trampenau, Migration enthalpies in FCC and BCC metals, J. Phys.: Condens. Matter **4**, 9321 (1992).

[58] L. Zhu, Z. Chen, W. Zhong, C. Wei, G. Cai, L. Jiang, Z. Jin, and J.-C. Zhao, Measurement of diffusion coefficients in the bcc phase of the Ti-Sn and Zr-Sn binary systems, Metall. Mater. Trans. A **50**, 1409 (2019).

[59] G. Kidson and J. McGurn, Self-diffusion in body-centered cubic zirconium, Can. J. Phys. **39**, 1146 (1961).

[60] C. Herzig and H. Eckseler, On the anomalous self-diffusion in ß-zirconium: Temperature dependence of the isotope effect, Int. J. Mater. Res. **70**, 215 (1979).

[61] J. Federer and T. Lundy, Diffusion of Zr95 and Cb95 in bcc zirconium, Trans. Metall. Soc. AIME **227**, 592 (1963).

[62] B. S. Hickman, The formation of omega phase in titanium and zirconium alloys: A review, J. Mater. Sci. **4**, 554 (1969).

[63] J. Towns, T. Cockerill, M. Dahan, I. Foster, K. Gaither, A. Grimshaw, V. Hazlewood, S. Lathrop, D. Lifka, G. D. Peterson, R. Roskies, J. R. Scott, and N. Wilkins-Diehr, XSEDE: Accelerating scientific discovery, Comput. Sci. Eng. **16**, 62 (2014).